Supplementary Information

Hierarchically porous PdO-functionalized SnO_2 nano-architectures for exclusively selective, sensitive, and fast detection of exhaled hydrogen

Sang Hun Kim,[‡a] Young Kook Moon,[‡a] Jong-Heun Lee,[§a] Yun Chan Kang[a] and Seong-Yong Jeong[*ab]

[a]*Department of Materials Science and Engineering, Korea University, Seoul 02841, Republic of Korea*

[b]*Department of Nanoengineering, University of California San Diego, 9500 Gilman Dr, La Jolla, CA 92122, USA*

[‡]*These authors contributed equally to this work.*

[§]*Deceased*

[*]*Corresponding author: S.-Y. Jeong*

Email: jeong7460@korea.ac.kr

EXPERIMENTAL SECTION

Gas-sensing characteristics. Before the gas-sensing characteristics were evaluated, the sensors were stabilized by annealing at 500 °C for 2 h. The sensors were placed in a specially designed quartz tube (1.5 mm^3), and the atmosphere was changed between air and analyte gas molecules using a 4-way valve. Gas-sensing characteristics of various gases (hydrogen: 20 ppm, ethanol: 1 ppm, acetone: 2 ppm, ammonia: 5 ppm, methane: 20 ppm, carbon monoxide: 20 ppm, and nitrogen monoxide: 0.05 ppm) were examined at a flow rate of 200 cm^3 min^{-1} and 300−450 °C under an RH of 80%. For this, the gas (25 °C and RH of 80%) was poured onto the sensor heated at 300−450 °C. The two-probe direct current (DC) resistance of the sensor was then measured using an electrometer (6487 picoammeter/voltage source, Keithley, USA) connected to a computer.

Material characterization. The crystal structure of the sensing material was investigated by performing X-ray diffraction (XRD, D/MAX-2500 V/PC, Rigaku, USA) with a CuKα radiation source (λ=1.5402 Å). The chemical states of the samples were investigated by employing X-ray photoelectron spectroscopy (XPS, X-TOOL, ULVAC-PHI Inc., Japan). The morphologies of the sensing materials were analyzed using field-emission scanning electron microscopy (FE-SEM; SU-70, Hitachi, Japan) and high-resolution transmission electron microscopy (HR-TEM; FEI, TALOS F200X, USA). The pore size distribution and surface area of porous SnO_2 spheres were determined using Brunauer–Emmett–Teller (BET) nitrogen adsorption/desorption analysis (Tristar 3000, Micromeritics Instrument Co., USA).

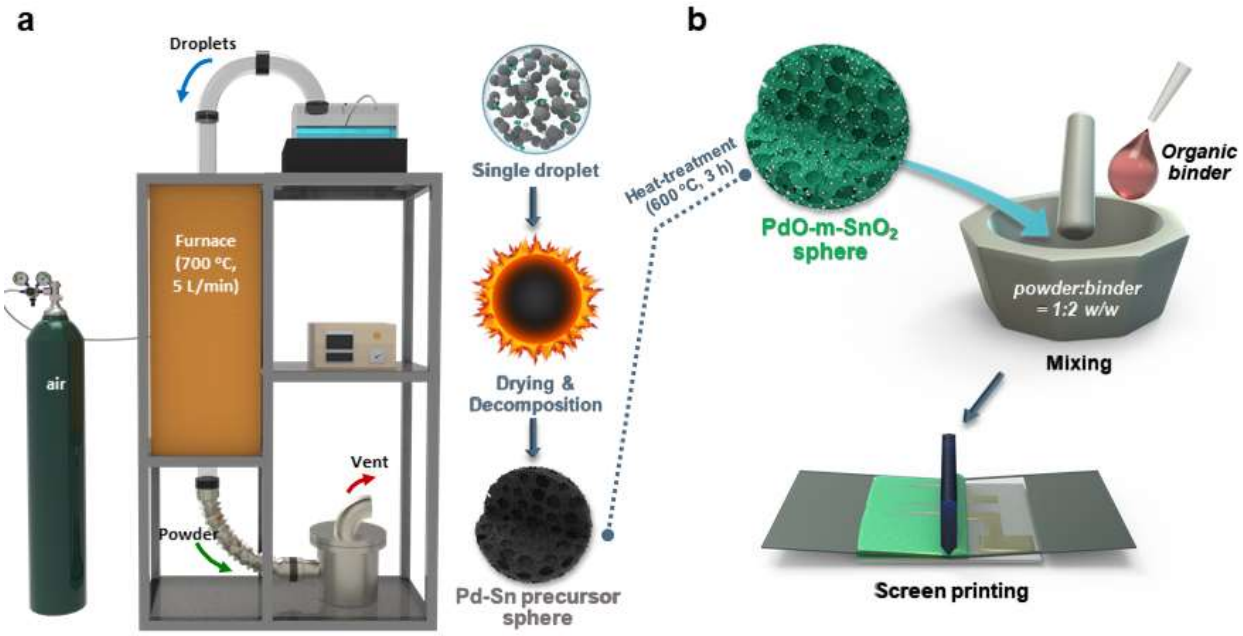

Figure S1. Schematics showing (a) the preparation of porous PdO-functionalized SnO_2 (PdO-m-SnO_2) spheres by ultrasonic spray pyrolysis and (b) sensor fabrication by screen printing of the slurry containing PdO-m-SnO_2 spheres.

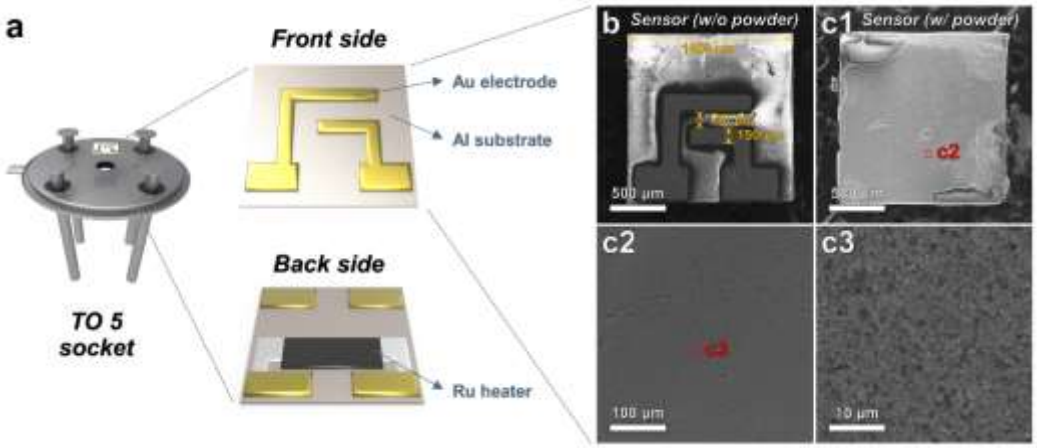

Figure S2. (a) Schematic illustration and (b, c) SEM images of sensor.

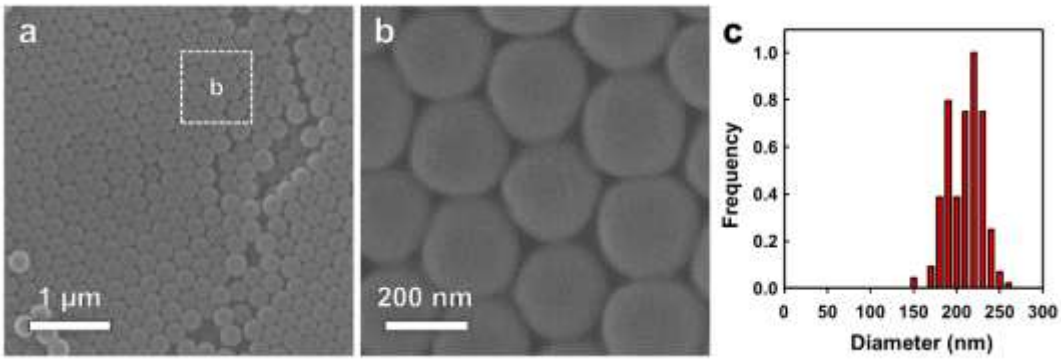

Figure S3. (a, b) SEM images and (c) particle-diameter distribution of polystyrene (PS).

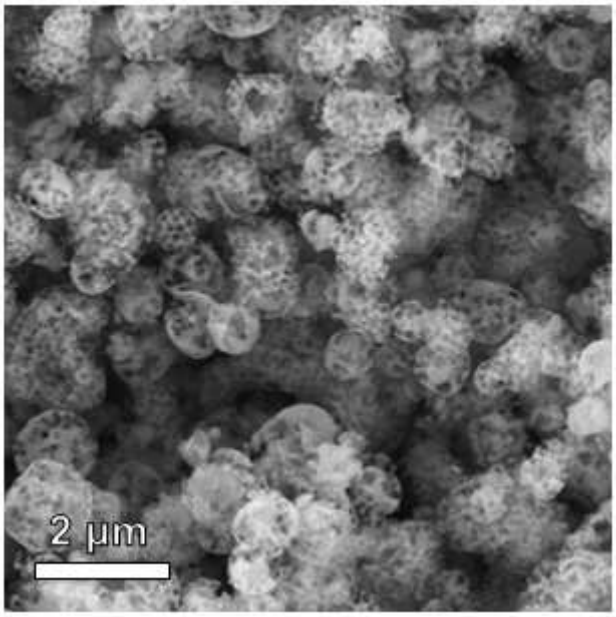

Figure S4. SEM image of the Pd-Sn precursor spheres.

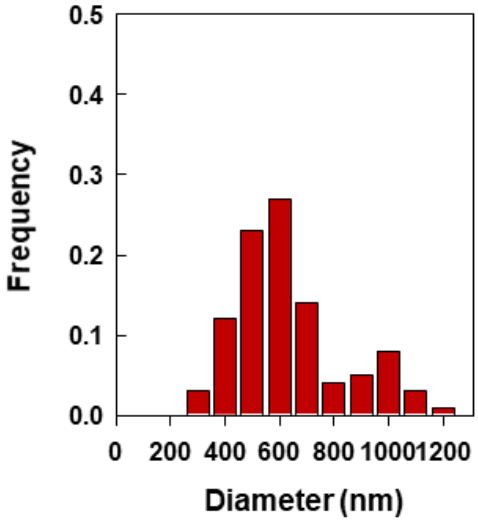

Figure S5. Particle-diameter distribution of PdO-m-SnO_2 spheres.

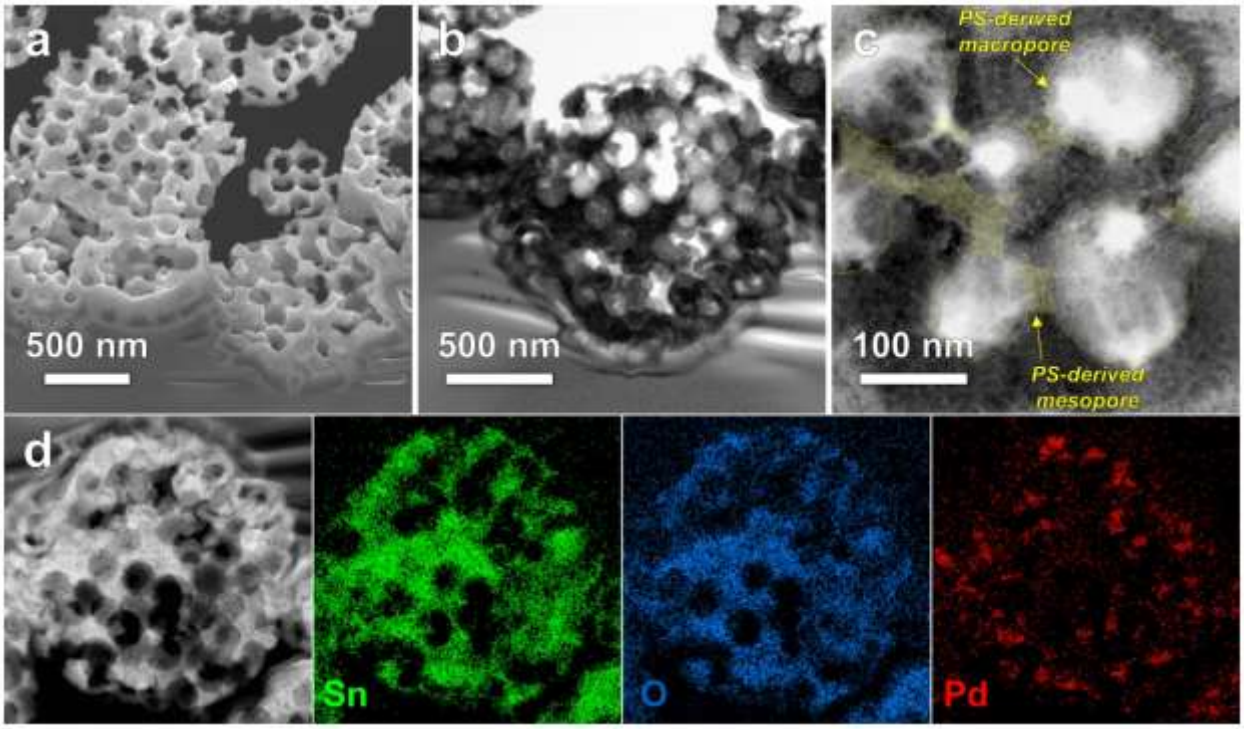

Figure S6. (a) Cross-sectional SEM, (b, c) TEM, and (d) EDS elemental mapping (Sn, O, and Pd) images of 0.1PdO-m-SnO_2.

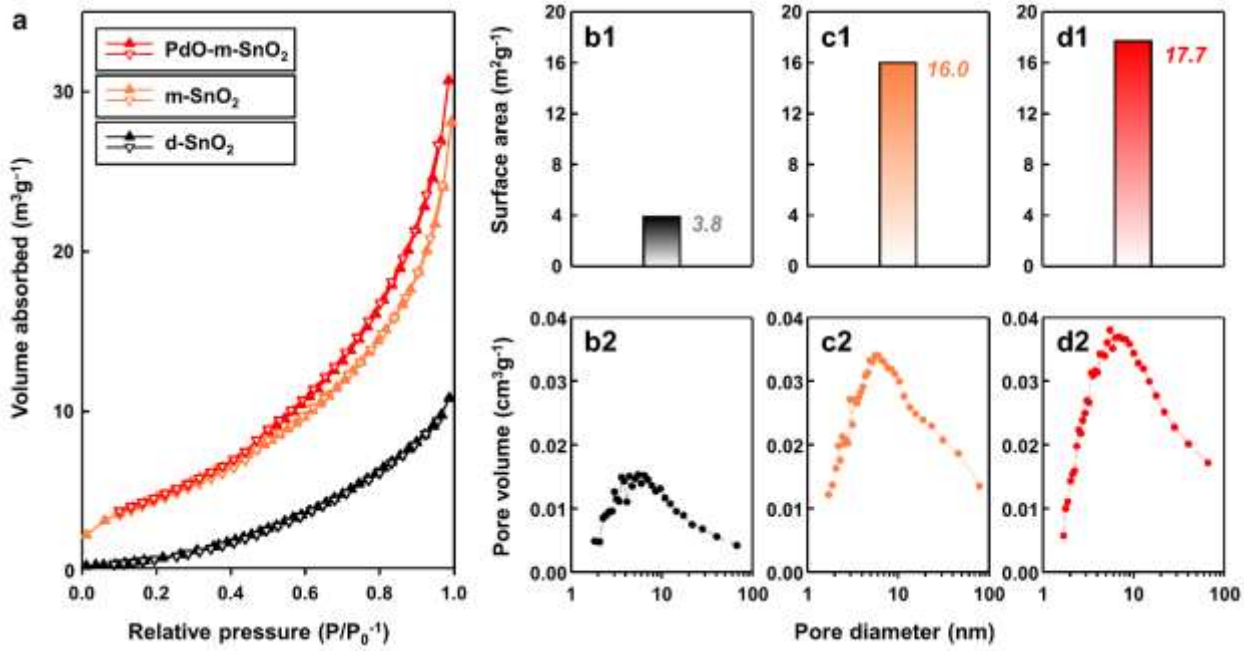

Figure S7. (a) Nitrogen adsorption/desorption isotherms of the d-, m-, and PdO-m-SnO_2 spheres. Specific surface area and pore size distribution of the (b) d-SnO_2, (c) m-SnO_2, and (d) 0.1PdO-m-SnO_2 spheres.

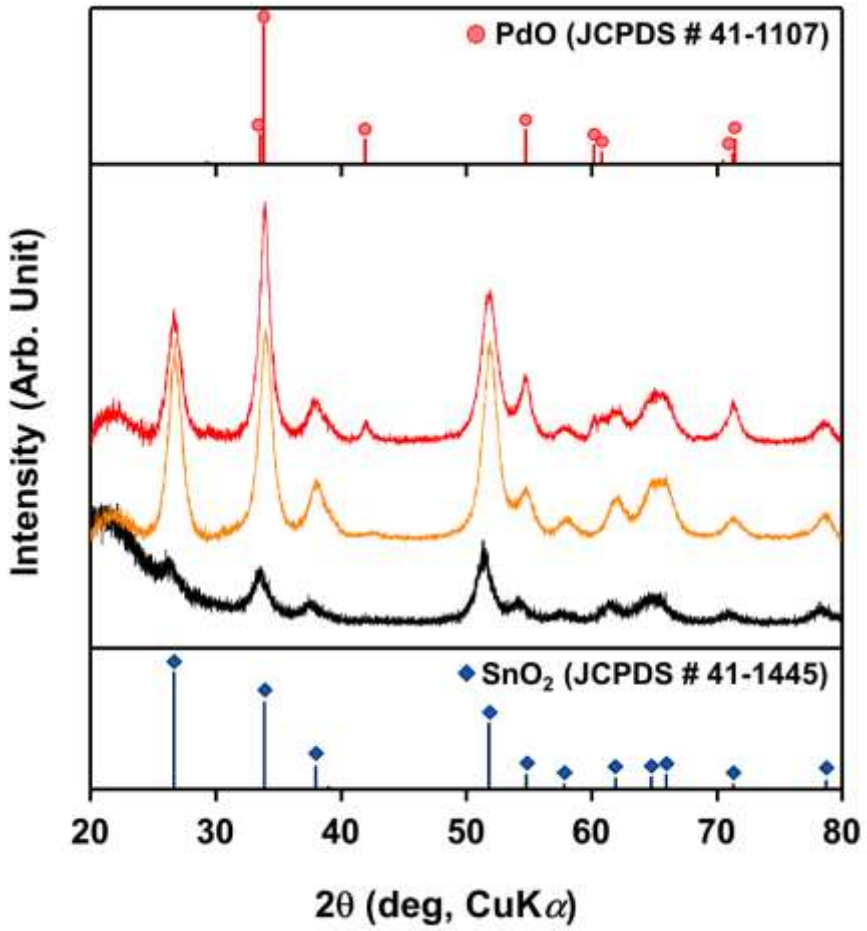

Figure S8. XRD patterns of d-SnO_2 (black), m-SnO_2 (orange), and 0.1PdO-m-SnO_2 (red) sensors.

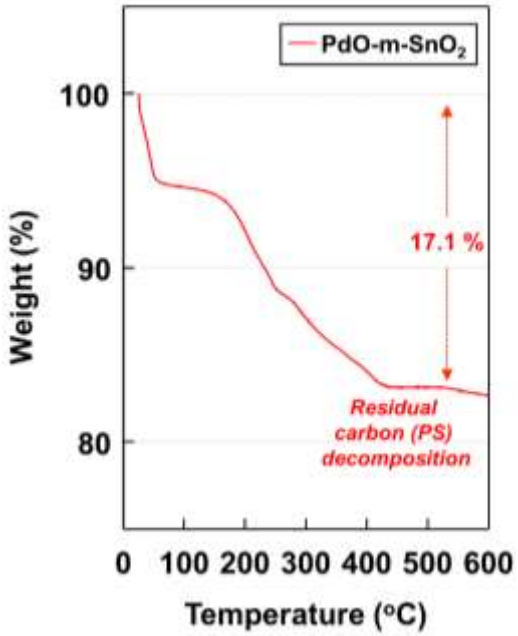

Figure S9. TGA curve of the 0.1PdO-m-SnO_2 sample.

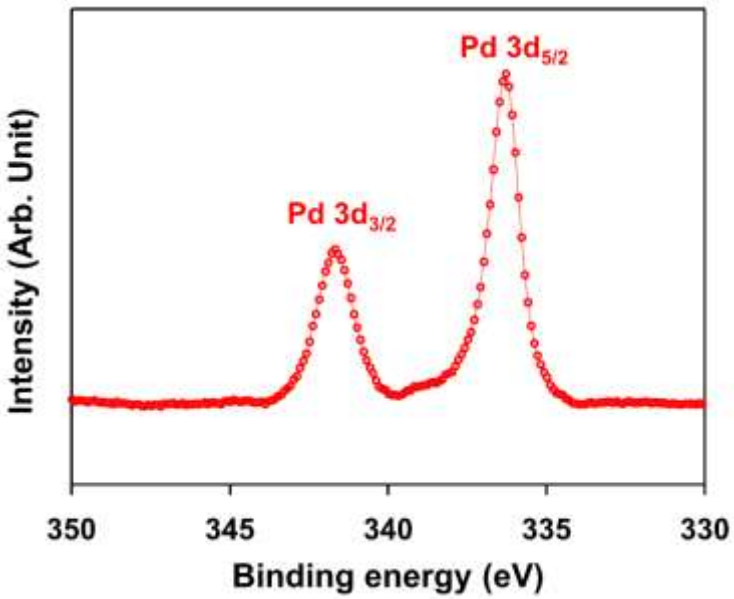

Figure S10. XPS spectra of Pd 3d for the 0.1PdO-m-SnO_2 sample.

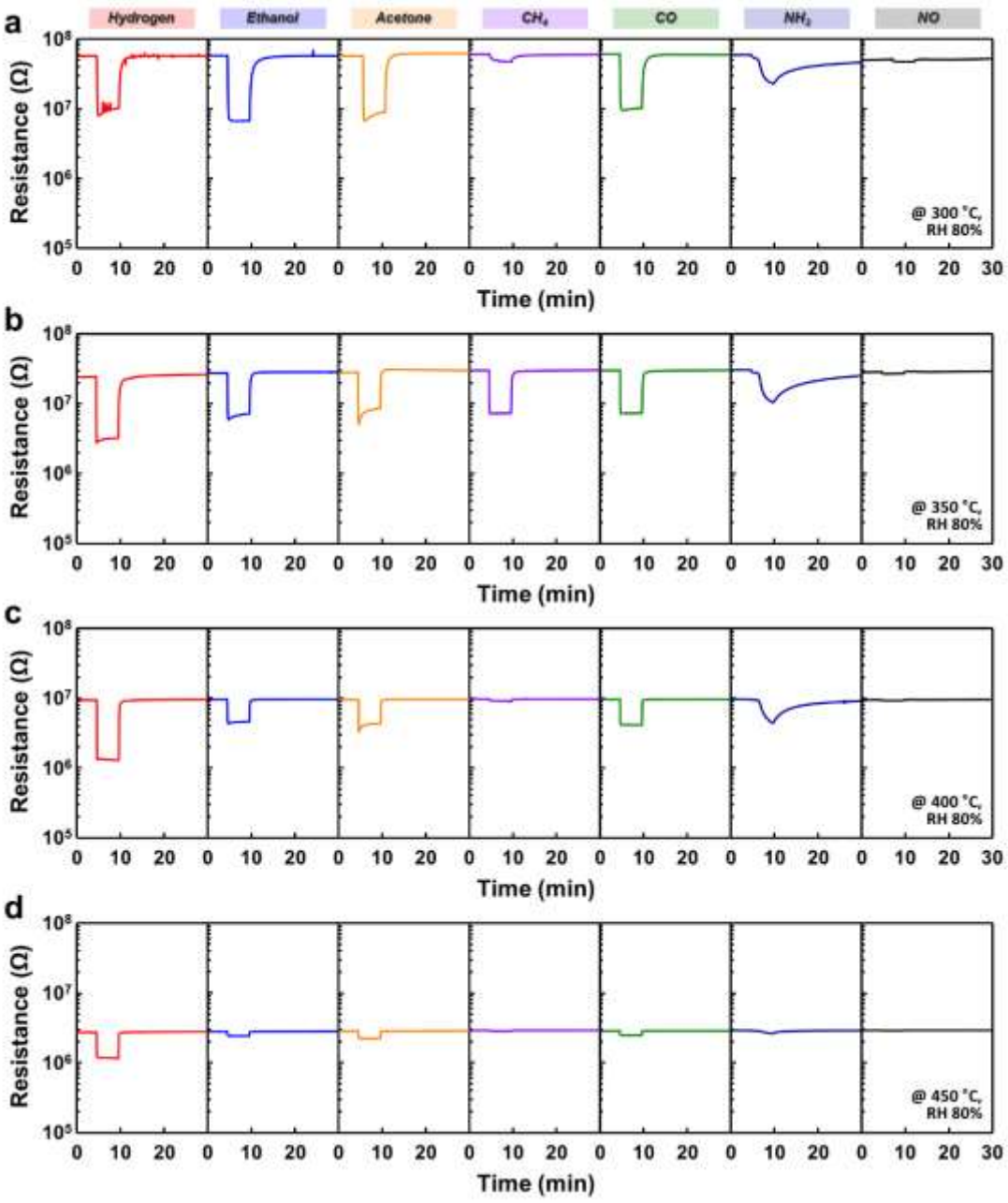

Figure S11. Dynamic sensing transients of the 0.1PdO-m-SnO_2 sensor at (a) 300, (b) 350, (c) 400, and (d) 450 °C (ambient RH: 80%).

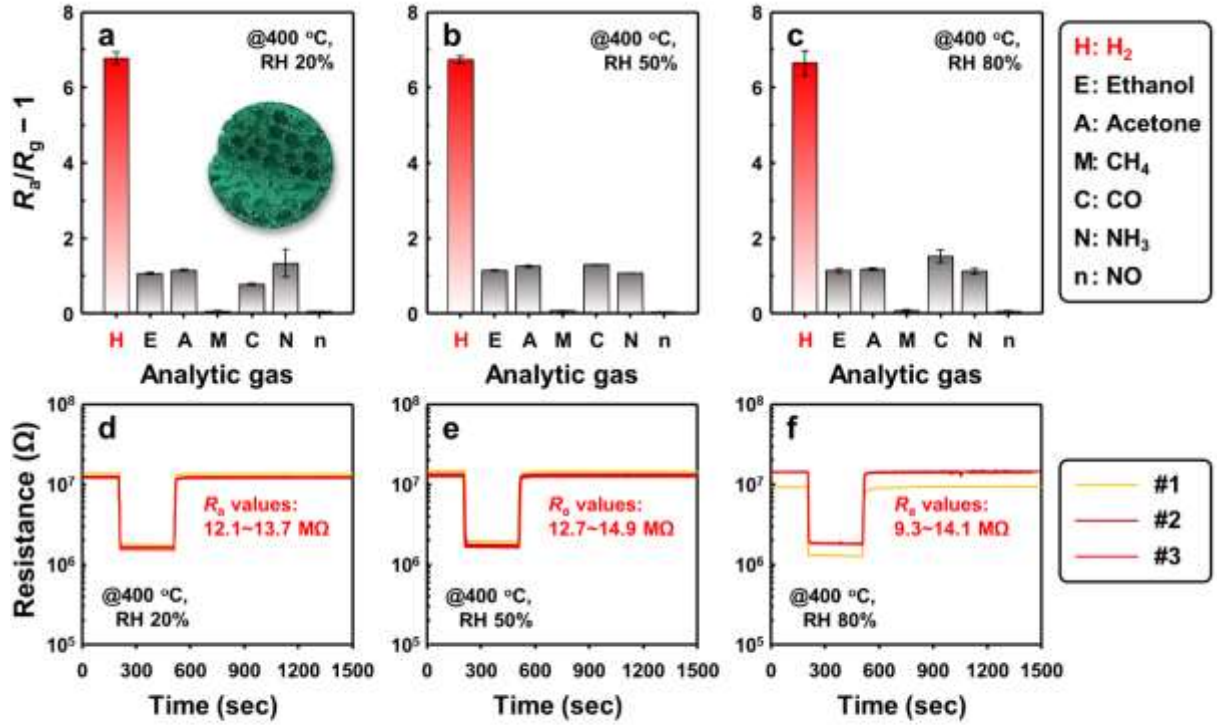

Figure S12. Gas responses and dynamic hydrogen sensing transients (at 400 °C) of 0.1PdO-m-SnO_2 sensor under different humidity conditions (humidity concentration: (a and d) RH 20 %; (b and e) RH 50 %; and (c and f) RH 80 %, concentration of the analyte gas molecules: H = 20 ppm, E = 1 ppm, A = 2 ppm, M = 20 ppm, C = 20 ppm, N = 5 ppm, n = 0.05 ppm, error bars indicate standard deviations for three sensors)

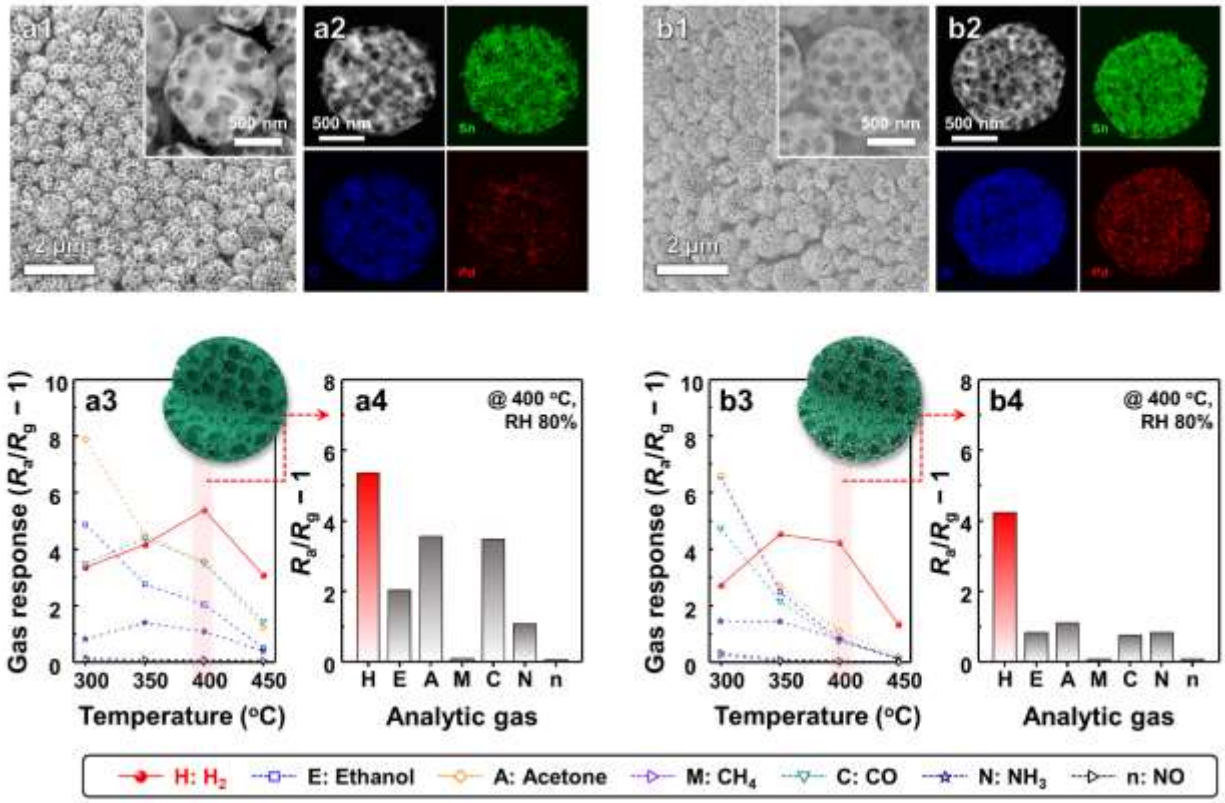

Figure S13. (a1) SEM and (a2) EDS elemental (Sn, O, and Pd) mapping images of 0.05PdO-m-SnO_2. (a3, a4) Gas-sensing characteristics and gas response of the 0.05PdO-m-SnO_2 sensor. (b1) SEM and (b2) EDS elemental (Sn, O, and Pd) mapping images of the 0.2PdO-m-SnO_2 sensor. (b3, b4) Gas-sensing characteristics and gas response of the 0.2PdO-m-SnO_2 sensor. (Analyte gas concentrations: H = 20 ppm, E = 1 ppm, A = 2 ppm, M = 20 ppm, C = 20 ppm, N = 5 ppm, and n = 0.05 ppm; temperature range: 300–450 °C; ambient RH: 80%).

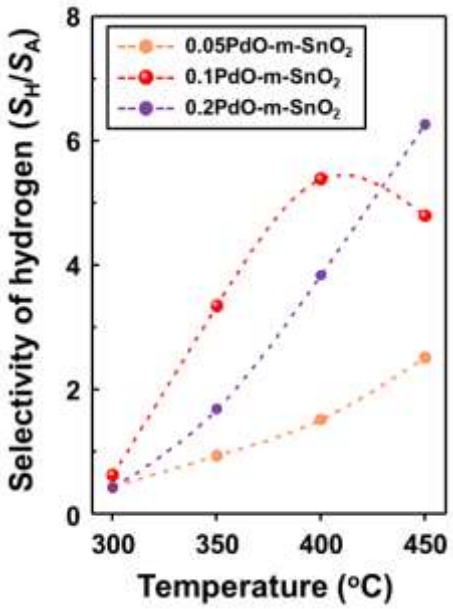

Figure S14. Hydrogen selectivity (S_H/S_A) of 0.05, 0.1, and 0.2PdO-m-SnO_2 (temperature range: 300–450 °C; ambient RH: 80%).

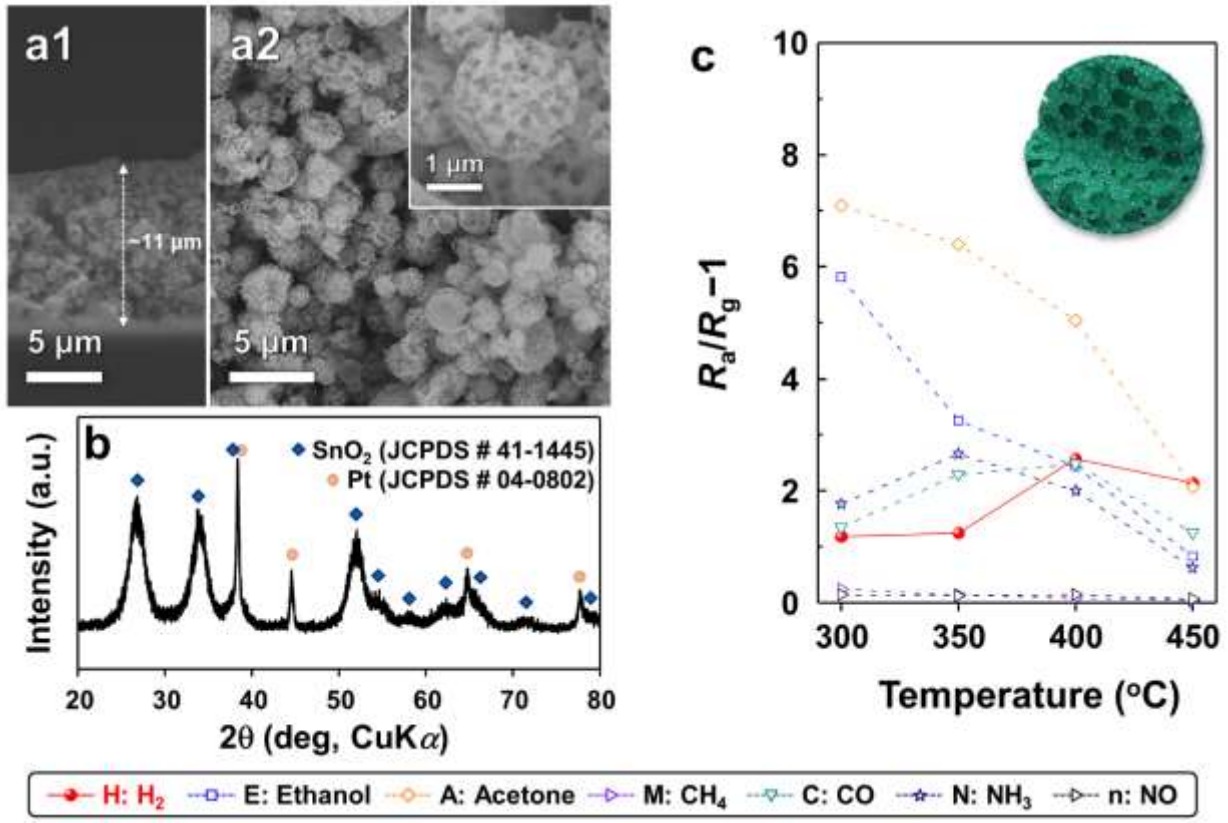

Figure S15. (a) SEM images, (b) XRD pattern, and (a) gas-sensing characteristics of Pt-m-SnO_2 (analyte gas concentrations: H = 20 ppm, E = 1 ppm, A = 2 ppm, M = 20 ppm, C = 20 ppm, N = 5 ppm, and n = 0.05 ppm; temperature range: 300–450 °C; ambient RH: 80%).

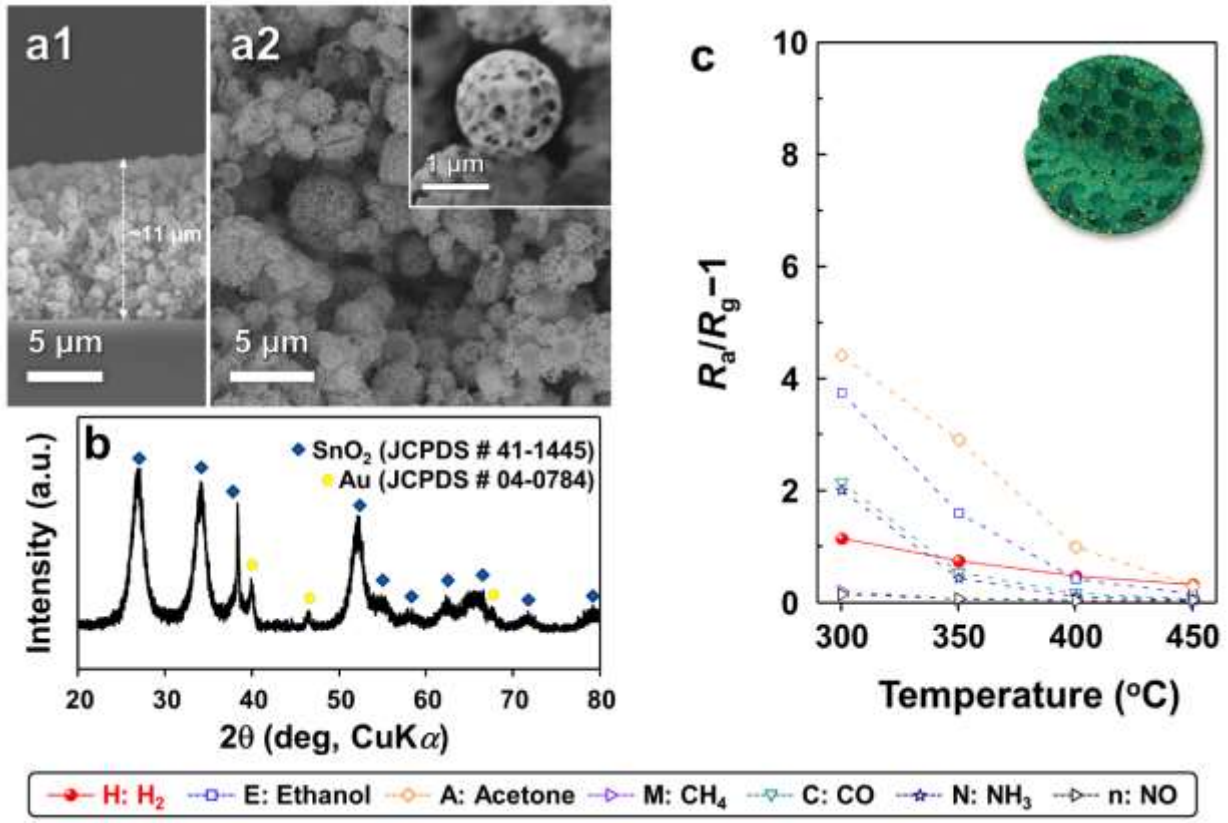

Figure S16. (a) SEM images, (b) XRD pattern, and (a) gas-sensing characteristics of Au-m-SnO_2 (analyte gas concentrations: H = 20 ppm, E = 1 ppm, A = 2 ppm, M = 20 ppm, C = 20 ppm, N = 5 ppm, and n = 0.05 ppm; temperature range: 300–450 °C; ambient RH: 80%).

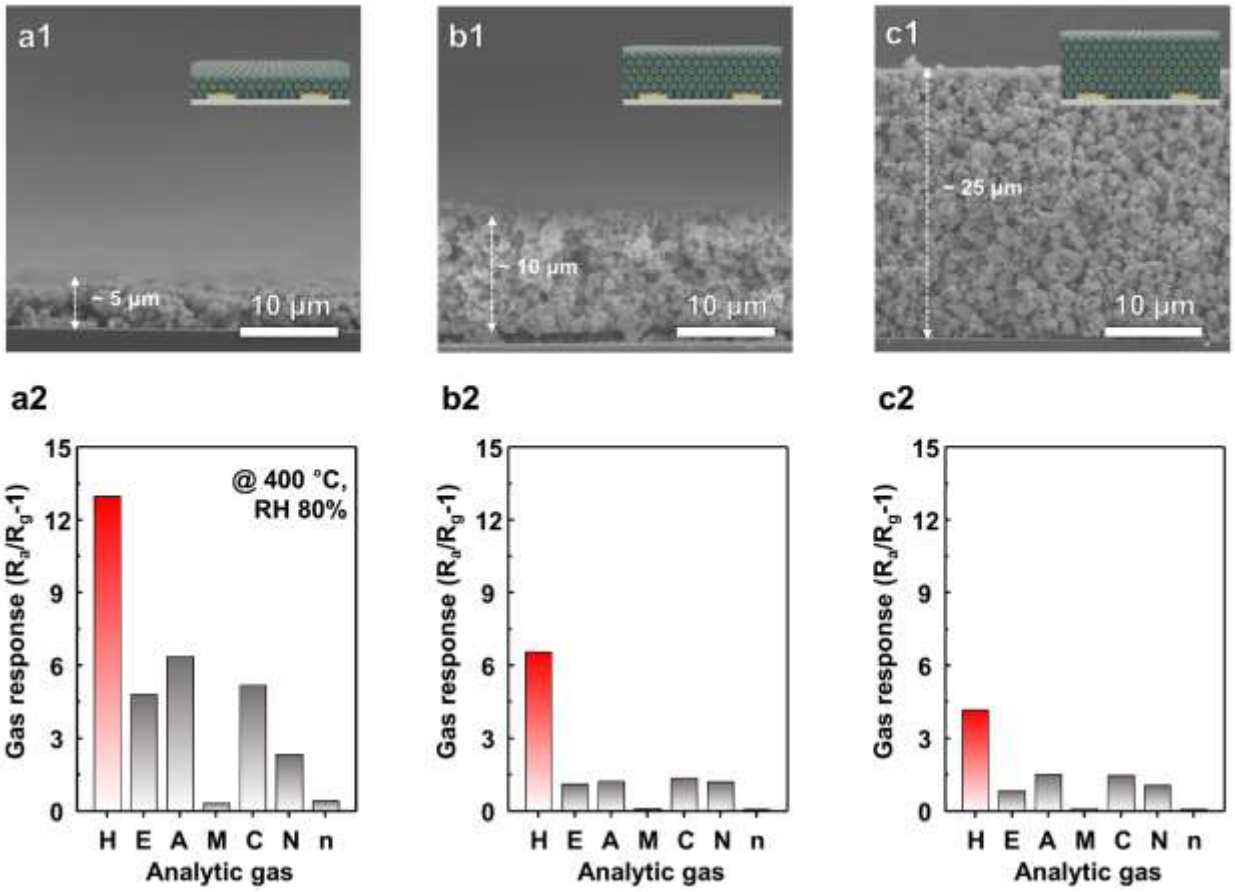

Figure S17. Cross-sectional SEM images and gas response of the (a) 5-µm-thick 0.1PdO-m-SnO_2, (b) 10-µm-thick 0.1PdO-m-SnO_2, and (c) 25-µm-thick 0.1PdO-m-SnO_2 sensing films (analyte gas concentrations: H = 20 ppm, E = 1 ppm, A = 2 ppm, M = 20 ppm, C = 20 ppm, N = 5 ppm, and n = 0.05 ppm; temperature range: 400 °C; ambient RH: 80%).

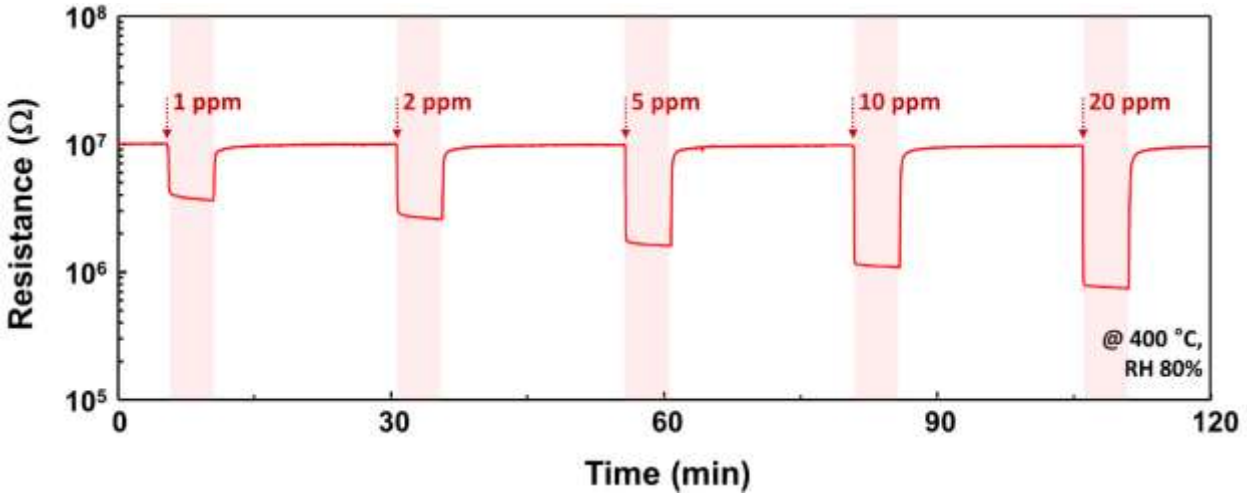

Figure S18. Dynamic gas-sensing transient of the 0.1PdO-m-SnO_2 sensor toward hydrogen mixed with simulated breath.

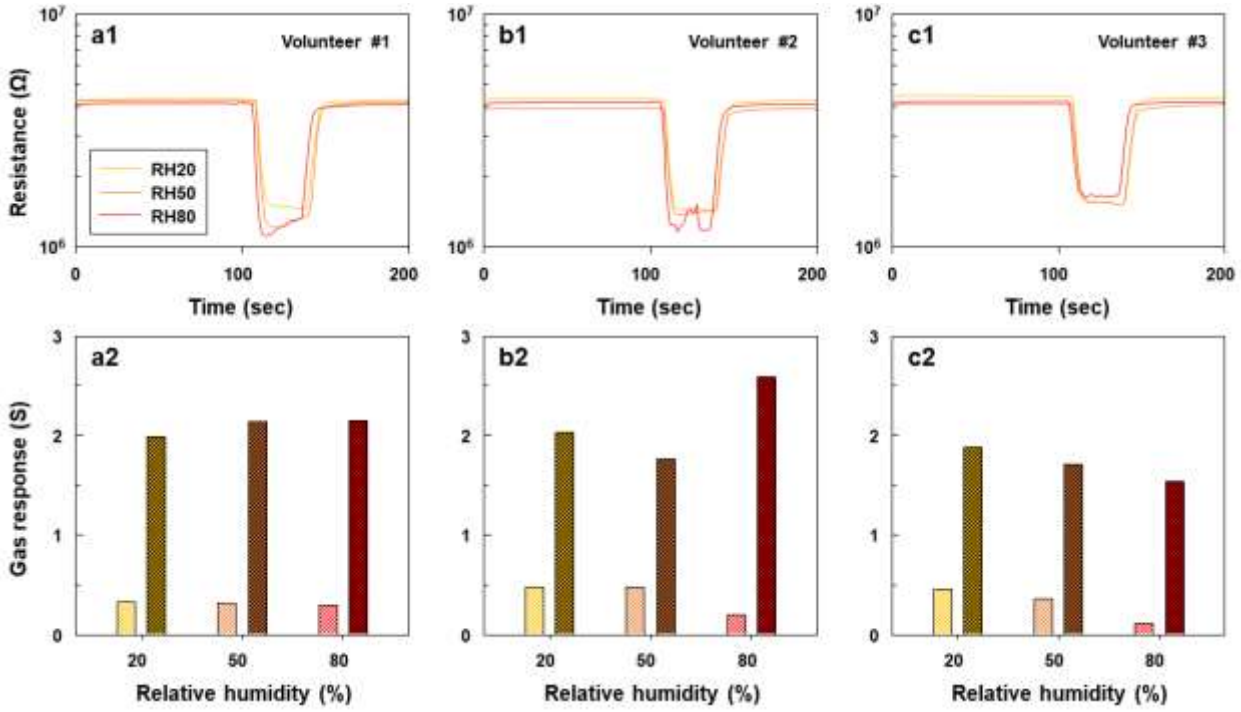

Figure S19. Gas sensing characteristics of 0.1PdO-m-SnO_2 sensor to the human breath with and without 20 ppm hydrogen at 400 °C.

Sensor measurement

The breath to the 3 volunteer was collected using a 20 L Tedlar bag. The simulated breath of healthy people was prepared by mixing the exhaled breath and 20 ppm hydrogen. Prior to the sensor measurement, the 0.1PdO-m-SnO_2 sensor was stabilized under humid air (RH 20 %, RH 50 %, and RH 80 %). The gas sensing characteristics of the sensor to both breaths were evaluated by changing the atmosphere from the humid air to the breaths (Fig. S17). The gas flow rate was fixed at 100 sccm and the breath exposure time was 30 s.

Table S1. Gas response comparison ($R_a/R_g - 1$) or ($R_g/R_a - 1$) of various sensing materials toward hydrogen detection as previously reported in the literature with the macroporous PdO-functionalized SnO_2 sensor proposed in this study.[S1–S13]

Materials	**H_2 conc. (ppm)**	**Response ($R_a/R_g - 1$) or ($R_g/R_a - 1$)**	**Detection limit (ppm)**	**Sensor temp. (°C)**	**Relative humidity (%)**	**$\tau_{res.}$ (s)**	**Ref.**
Pd-decorated crumpled rGO composites	200000	0.15	25	RT	95	73.0	[S1]
Half-pipe Pd nanotube networks	14000	0.01	90	RT	60	12.0	[S2]
ZnO-SnO_2 composites	10000	0.9		150	30	60.0	[S3]
Imidazolium-functionalized triptycene polyether sulfone-PdPt	10000	0.0756	0.4	RT	50	92	[S4]
Pt@NiO core–shell nanostructures	5000	3.23	1500	RT	70	87	[S5]
WO_3-decorated ZnO nanowires	2000	11.6		200	0	~200	[S6]
Anodic niobium oxide nanorods	1000	16		180	0	240.0	[S7]
Pd@Pt yarn fiber	1000	0.0065	2	RT	80	44	[S8]
SnO_2-Co_3O_4 nanoparticles	500	3.5	20	350	0		[S9]
Pt thin films	200	0.04	0.5	150	90	120.0	[S10]
Mesoporous $Sn_{0.9}Ce_{0.1}O_{2-\delta}$ composites	150	3	40	350	0		[S11]
Pd-SnO_2 thin films	100	2.1		180	80	50.0	[S12]
Mesoporous Co-doped TiO_2 structures	100	~1.0	50	RT	30	66.0	[S13]
Hierarchically PdO-functionalized SnO_2 spheres	**20**	**6.3**	**0.096**			**4.0**	**This work**

REFERENCES

S1 M. M. Mohammadi , A. Kumar , J. Liu , Y. Liu , T. Thundat and M. T. Swihart, *ACS Sens.* 2020, **5**, 2344–2350.

S2 M. Cho, J. Zhu, H. Kim, K. Kang and I. Park, *ACS Appl. Mater. Interfaces* 2019, **11**, 13343–13349.

S3 B. Mondal, B. Basumatari, J. Das, C. Roychaudhury, H. Saha and N. Mukherjee, *Sens. Actuators, B* 2014, **194**, 389–396.

S4 W.-T. Koo, Y. Kim, S. Kim, B. L. Suh, S. Savagatrup, J. Kim, S.-J. Lee, T. M. Swager and I.-D. Kim, *Chem* 2020, **6**, 2746–2758.

S5 C.-H. Wu, Z. Zhu, H.-M. Chang, Z.-X. Jiang, C.-Y. Hsieh and R.-J. Wu, *J. Alloys Compd.* 2020, **814**, 151815.

S6 S. Park, *Mater. Lett.* 2019, **234**, 315–318.

S7 Z. Pytlicek, M. Bendova, J. Prasek and A. Mozalev, *Sens. Actuators, B* 2019, **284**, 723–735.

S8 D.-H. Kim, S.-J. Kim, H. Shin, W.-T. Koo, J.-S. Jang, J.-Y. Kang, Y. J. Jeong and I.-D. Kim, *ACS nano* 2019, **13**, 6071–6082.

S9 X.-T. Yin, J. Li, D. Dastan, W.-D. Zhou, H. Garmestani and F. M. Alamgir, *Sens. Actuators, B* 2020, **319**, 128330.

S10 T. Tanaka, S. Hoshino, T. Takahashi and K. Uchida, *Sens. Actuators, B* 2018, **258**, 913–919.

S11 S. Somacescu, P. Osiceanu, J. M. C. Moreno, L. Navarrete and J. M. Serra, *Micropor. Mesopor. Mater.* 2013, **179**, 78–88.

S12 N. Van Duy, T. H. Toan, N. D. Hoa and N. Van Hieu, *Inter. J. Hydro. Energy* 2015, **40**, 12572–12580.

S13 Z. Li, A. A. Haidry, T. Wang and Z. J. Yao, *Appl. Phys. Lett.* 2017, **111**, 032104.